The 2010 IEEE/RSJ International Conference on
Intelligent Robots and Systems
October 18-22, 2010, Taipei, Taiwan

Investigation on Pretensioned Shape Memory Alloy Actuators for Force and Displacement Self-Sensing

Chao-Chieh Lan, *Member*, *IEEE&ASME*, Chen-Hsien Fan

***Abstract* –This paper investigates and realizes the self-sensing capability of shape memory alloy (SMA) actuators. SMA exhibits large stroke, high energy density, and requires low driving voltage. To make SMA more applicable to small scale robotic manipulations, its motion control using accurate self-sensing is necessary. The presented technique builds a self-sensing model by measuring the SMA electrical resistance. Effects of pretension force on strain and force self-sensing are investigated. The model is polyfitted to replace sensor electronics for strain or force feedback. A pretensioner is specifically designed to provide sufficient pretension force without affecting the subject to be actuated. The advantages gained from using polyfitted self-sensing models are demonstrated through several step response control experiments. With the merits shown, we expect this technique can be utilized for SMA actuators in meso to micro scale applications.**

Index Terms – Shape memory alloy, self-sensing actuators, flexural manipulator, hysteresis model.

I. Introduction

To meet the demanding applications of miniature robotic manipulations, many unconventional actuators have been developed. They include thermal [1–2], pneumatic [3], ionic polymer metal composite [4], piezoelectric [5], magnetic [6], and shape memory alloy (SMA) [7–8] actuators. These actuators are characterized by their energy density, specific power, and ease of fabrication. Key to the successful implementation of these actuators is how easy it is to sense the actuator outputs so their motion can be precisely controlled. Considering compactness and cost, it is beneficial and sometimes necessary to reduce the number of additional sensing devices required for actuators.

Depending on the actuation principles, various approaches have been used to reduce or even eliminate the need of sensors. One approach is to install embedded sensors [1–2] without increasing the dimension of actuators. Another approach is to seek a predictive model so that output variables of an actuator can be solely determined by its input variables. This approach works well for voice coil actuators [9]. The third approach is self-sensing, which takes advantage of the inherent electrical variables of the actuator to infer its mechanical variables. The use of self-sensing completely removes the complexity and cost introduced by additional sensors. Examples include piezoelectric [10], polymer [11], and electromagnetic actuators [12]. To obtain accurate sensing, there must exist deterministic relations between the measured variable and controlled variable of the actuator.

SMA actuators have very high energy density, silent operation, and are miniaturizable. Compared with other actuators, their self-sensing capability has not yet been successfully explored. When being heated, SMA changes its shape through metallographic transformation. For slender wire type SMA with proper initial tension, the shape change results in a significant reduced wire length of approximately 5% strain. The length variation also results in (electrical) resistance variation. However, the mathematical modeling of SMA resistance to strain has not been seen in the literature, as compared to the models of temperature to strain [13–15]. Nevertheless, the use of resistance as sensor to realize self-sensing capabilities has been studied by several authors [16–18]. The remaining challenge of resistance-based SMA self-sensing is the accuracy of the predictive hysteresis model, along with its robustness to external disturbance.

This paper aims to investigate and realize the self-sensing capability of SMA wire actuators using their measurable electrical resistance. In Sec. II, the feasibility of force and strain self-sensing are compared. Effects of wire diameter and pretension force on hysteresis gaps are investigated. In Sec. III, the hysteresis gap between heating and cooling is conveniently modeled by using polynomials. Illustrative self-sensing step control experiments are conducted. For practical applications, a robotic flexural finger is demonstrated in Sec. IV that utilizes displacement self-sensing for manipulation control.

II. Force and Displacement Hysteresis Curves

2.1 Experiment setup

Fig. 1 shows the experiment setup where a load cell (Futek LSB 200) is connected on the two ends of a V-shaped SMA wire. The force at the load cell is the sum of the two ends and is denoted as the total force F_T. It includes the pretension force F_p and contraction force F. The wire connects to a helical bias spring with spring constant 588.60 N/m. A linear variable differential transformer (LVDT) measures the wire strain and spring displacement. The spring provides the wire with a tension force. The linear stage adjusts the pretension force in the wire given by the spring. A circuit has been set up in Fig. 2 to measure the wire resistance. When being actuated, the resistance of SMA wire is computed as

$$R_{SMA} = (V_{SMA}/V_R) \times R \tag{1}$$

To ensure that the voltage heating SMA wire is desirable, we use a buffer amplifier circuit to amplify the input signal. The actual voltage across the SMA wire V_{SMA} and the external resistor V_R are measured using a data acquisition card (NI

This work was supported in part by the National Science Council of Taiwan (with Project No. NSC 97-2221-E-006-069-MY2).

C.-C. Lan and C.-H. Fan are with the Department of Mechanical Engineering, National Cheng Kung University, No. 1, University Rd., Tainan, Taiwan. (corresponding author e-mail: cclan@mail.ncku.edu.tw).

DAQ PCI-6229). For an overall V-shaped length of 14 cm, three different wire diameters are studied. Their corresponding properties are listed in Table 1.

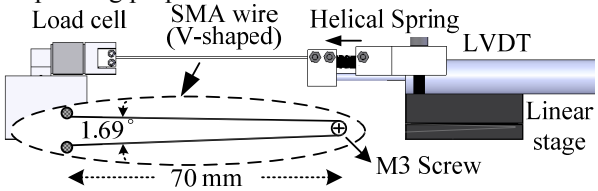

Fig. 1 Diagram of experiment setup

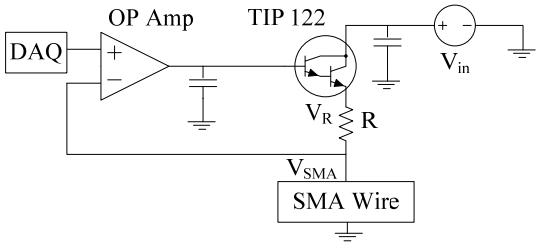

Fig. 2 Buffer amplifier circuit

Table 1 Properties of SMA wires [19]

Wire diameter d (μm)	100	125	200
Linear resistance (Ω/m)	126	75	29
Maximal allowable force (N)	4.601	7.220	18.247
Nominal force (N)	0.275	0.422	1.079

Using a sine wave voltage input with 1/90 Hz and amplitude 3.2 V, the strain to voltage (S-V) relation is shown in Fig. 3(a). This is very similar to the strain to temperature curve since voltage change is very slow. When the SMA wire is heated above an activation temperature, it transforms from martensite to austenite phase, resulting in a strain change. When cooled, it transforms back to its martensite phase and recovers its original length due to the spring force. As can be seen, the S-V relation exhibits a significant hysteresis gap. Regardless of the approach to model the hysteresis, the difference between heating and cooling paths adversely affects precision control of SMA. Smaller voltage amplitudes (2.9 V and 2.75 V) result in two smaller hysteresis loops inside the major loop. Fig. 3(b) further shows the strain to resistance (S-R) relation of the same experiment in Fig. 3(a). Unlike strain to temperature or strain to voltage curves that exhibit a large gap between heating and cooling paths, the gap of S-R hysteresis curves is much smaller. Hence we use the electric resistance of SMA wire as the feedback signal to realize SMA self-sensing capabilities.

In Fig. 3(b), the strain is proportional to resistance from A to B, and inversely proportional from B to C. Segment AB only slightly changes the strain and can be ignored. Therefore the hysteresis analysis focuses on Segment BC, which is roughly 85% of the entire strain. Segment BC can be utilized to obtain the strain signal from resistance. The same experiment can be conducted for contraction forces.

2.2 Effect of pretension force on the hysteresis gaps

Reducing the hysteresis gap is a major subject for accurate self-sensing. The force and strain of SMA wire can both be measured from the experiment setup in Sec. 2.1. To find out the effect of pretension force on the gap of strain curve and force curve of different SMA wires, we define the strain gap

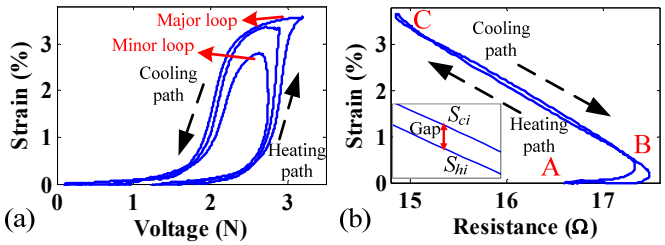

Fig. 3(a) Hysteresis loop of strain to voltage
(b) Hysteresis loop of strain to electric resistance

and force gap as follows.

$$\text{strain gap} = \frac{1}{k}\sum_{i=1}^{k}\left|S_{hi} - S_{ci}\right| / S_{\max} \times 100\% ;$$
$$\text{force gap} = \frac{1}{k}\sum_{i=1}^{k}\left|F_{hi} - F_{ci}\right| / F_{\max} \times 100\% \quad (2)$$

At the same resistance, the values S_{hi} and S_{ci} are the strain on the heating path and cooling path, respectively. When divided by the maximal strain $S_{\max}$ and maximal contraction force $F_{\max}$, the strain and force gaps measure the normalized average difference between the heating and cooling paths. The smaller the gap, the smaller the discrepancy between heating and cooling paths is. Thus it is a better candidate as a self-sensing model. By using the definitions in Eq. (2), Fig. 4 shows the S-R curve of d = 125 μm for different pretension forces. Starting at F_p = 1.70 N, the strain gap reduces from 8.196% to 2.702% at F_p = 4.67 N. The strain gap of the largest pretension force is almost zero.

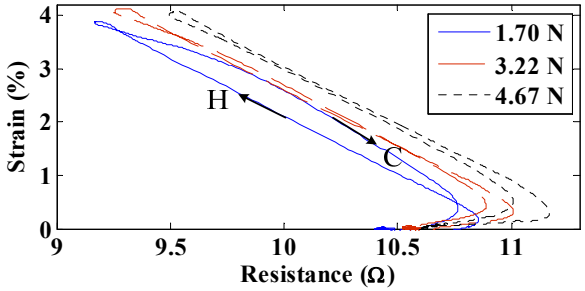

Fig. 4 Strain to resistance with different F_p's (d = 125 μm)

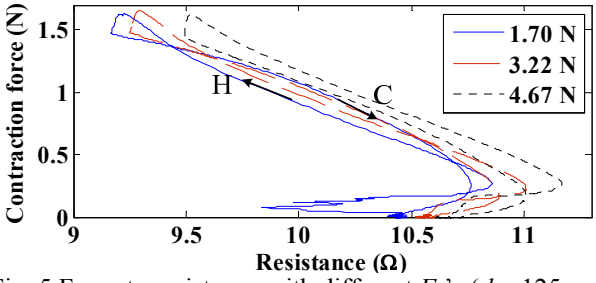

Fig. 5 Force to resistance with different F_p's (d = 125 μm)

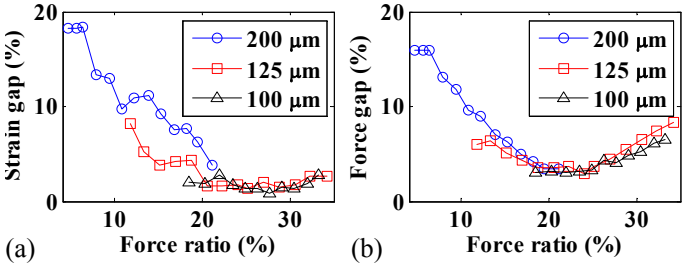

Fig. 6 (a) Strain gap versus force ratio
(b) Force gap versus force ratio

Fig. 5 shows the *F-R* curve for different pretension forces. Although the force gap reduces similarly for larger pretension forces, the value of the force gap is still significant. At F_p = 3.22 N, the force gap is the smallest 3.639%. Note that as the pretension force increases, the heating path gradually moves closer to the cooling path and then moves away.

The same experiment has been performed for d = 100 μm and d = 200 μm. Fig. 6(a) shows the strain gap of the three different wires at different pretention forces. For clear comparison, we define force ratio as the pretension force F_p divided by the maximal allowable force (indicted in Table 1) of a SMA wire. It is seen that the strain gap is smaller for smaller wire diameters. Comparing Figs. 6(a) and 6(b), the *S-R* curves can be tuned to exhibit the smallest gap and thus are better candidates for self-sensing when compared with the *F-R* curves.

2.3 Effect of changing stiffness on hysteresis curves

The above studies were performed by using springs of a constant stiffness. In practice, the spring may age or its spring constant may change due to environmental effects. In other words, SMA actuators may have to interact with spring loads of different stiffness. Fig. 7 shows a 100 μm wire with F_p = 1.70 N that experiences three substantially different stiffnesses. The difference among the three *S-R* curves is minimal. The corresponding three *F-R* curves are shown in Fig. 8, which obviously deviates from one another.

Summarizing the findings in Sec. 2.2 and 2.3, the *S-R* curves are better alternatives for self-sensing. Especially for smaller wire diameters and larger pretension forces, the gaps between heating and cooling paths are smaller.

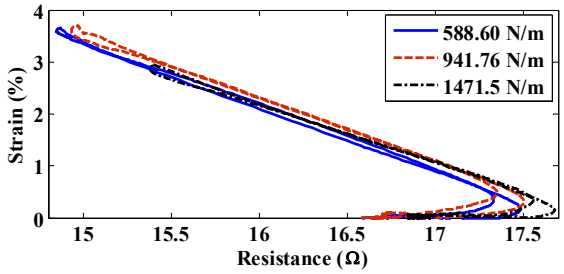

Fig. 7 *S-R* curves for different stiffnesses (F_p=1.70N; d =100 μm)

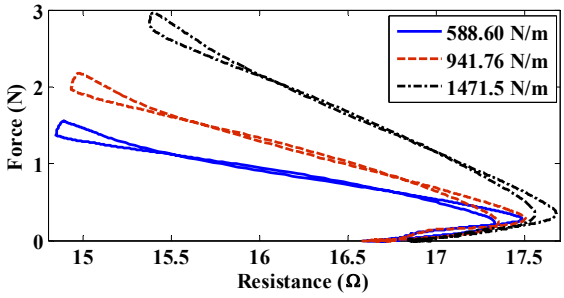

Fig. 8 *F-R* curves for different stiffnesses (F_p=1.70 N; d = 100 μm)

III. Self-sensing Control Using Polynomial Models

From Sec. II, we know that strain self-sensing is a better option compared to force self-sensing. To convert electric resistance into strain in the feedback control system, we need to establish an *S-R* model to provide strain information by sensing the SMA resistance. Sophisticated hysteresis models (e.g., Refs. [20-21]) have been widely found in the literature. However, since the heating and cooling paths are so close to each other, a polynomial model is sufficient to describe the *S-R* relation. In Fig. 3(b), the strain curve from B to C is divided into the heating and cooling paths. A normalized resistance λ is introduced.

$$\lambda = (R - R_{\min})/(R_{\max} - R_{\min}) \tag{3}$$

where $R_{\max}$ and $R_{\min}$ are the maximal and minimal resistances from B to C. The approximate functions for the heating and cooling paths are denoted as:

$$S_h = g_h(\lambda); S_c = g_c(\lambda) \tag{4}$$

We use the MATLAB® "polyfit" function to obtain the parameters of the polynomial model. To provide sufficient accuracy, we choose sixth order polynomials in our analysis.

Fig. 9 shows the sixth order polynomial fits together with the experimental *S-R* curve. In the curve we have $R_{\min}$ = 15.1526 Ω and $R_{\max}$ = 17.4945 Ω. Explicit forms of the polynomials are given inside Fig. 9. The strain gap of this curve is 1.2172%. Since the heating and cooling paths are very close to each other, a simple yet practical means to reconstruct the *S-R* relation is to average the two curves. Thus the required R of a desired S is given as follows and the average curve is plotted in Fig. 9.

$$S = g_a(\lambda) = [g_h(\lambda) + g_c(\lambda)]/2 \tag{5}$$

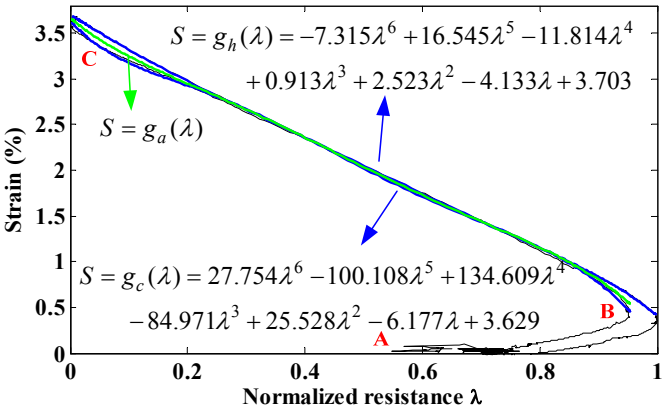

Fig. 9 Polynomials and actual curves (F_p=1.9 N; d=100 μm)

Using the polynomial model to obtain the feedback signal, we implement a PID controller to further control the strain. To adapt to the highly nonlinear SMA actuator, the gains of the PID controllers are auto-tuned by fuzzy logic rules. The fuzzy rules determine the appropriate values of K_P, K_I and K_D. The fuzzy ratios K_P', K_I' and K_D' are determined by a fuzzy method. The ranges of K_P, K_I and K_D are defined as [$K_{P\min}$ $K_{P\max}$], [$K_{I\min}$ $K_{I\max}$] and [$K_{D\min}$ $K_{D\max}$]. The relationships of PID parameters and fuzzy ratios are expressed as

$$\begin{aligned} K_P &= (K_{P\max} - K_{P\min}) \times K_P' + K_{P\min} \\ K_I &= (K_{I\max} - K_{I\min}) \times K_I' + K_{I\min} \\ K_D &= (K_{D\max} - K_{D\min}) \times K_D' + K_{D\min} \end{aligned} \tag{6}$$

Fig. 10 shows the fuzzy PID control diagram. The parameters of PID controller are based on the values of error e and change in error e', and are tuned between K_P = 0.01~0.11, K_I = 0.02~0.06 and K_D = 0.0005~0.001. The input voltage is determined by the error, change in error and fuzzy-tuned PID

gains. When the value of actual strain changes, the change of SMA resistance will be measured and converted to strain.

Fig. 11 shows the results of step response experiment where the increment of each step is 0.3% strain in six seconds. As can be seen, the resistance converted strain and actual strain (measured by LVDT) are very close to each other. For each desired strain, the value of the required electric resistance is converted from Eq. (5). The corresponding strain of heating (S_h) and cooling (S_c) are then calculated from Eq. (4). These values are detailed in Table 3. To study the difference between the desired strain and actual strain, we define the mean absolute error of each step response as

$$MAE = \frac{1}{n}\sum_{i=1}^{n} \left| S_i - S_{des} \right| / S_{des} \times 100\ \% \qquad (7)$$

where S_{des} is the desired strain at each step; S_i is the actual strain measured sequentially after one second of each step (till the end of each step). The last two rows of Table 2 indicate the detailed value of *MAE*. The maximal *MAE* is 2.619% at S_{des} = 1.5% (return). For other desired strains, the *MAE* is less than 2%. The small measuring error proves the effectiveness of self-sensing. Fig. 12 further shows the trace of strain to resistance relation during the step control experiment in Fig. 11. The points are recorded every 0.05 seconds.

Since the hysteresis curve depends on the pretension force and the diameter/length of the wire, a different polynomial model needs to be constructed for a specific wire. The effort to construct the model is minimal; the reasons being that only one hysteresis curve analysis is required and the polynomials can be efficiently integrated into the control system.

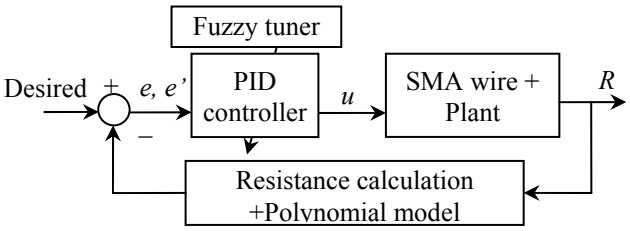

Fig. 10 Fuzzy PID control block diagram

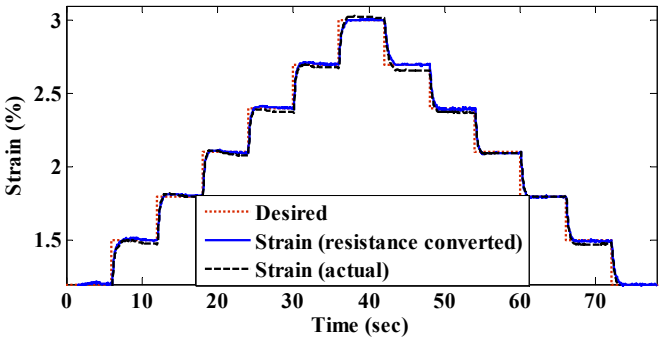

Fig. 11 Step response (F_p = 1.9 N; d = 100 μm)

Table 2 Numerical results of Fig. 11

Desired S (%)	1.5	1.8	2.1	2.4	2.7	3
Required R	16.737	16.497	16.274	16.055	15.825	15.577
$S_h = g_h(\lambda)$	1.506	1.819	2.112	2.398	2.697	3.034
$S_c = g_c(\lambda)$	1.493	1.781	2.088	2.402	2.703	2.966
MAE-rise (%)	1.032	1.020	1.071	0.741	1.000	1.640
MAE-return (%)	2.619	2.000	0.238	0.476	1.250	

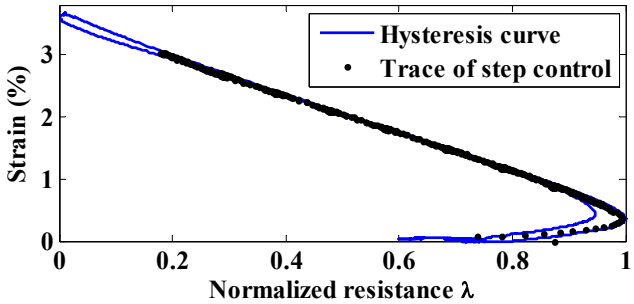

Fig. 12 Trace of *S-R* relation during the step response control

IV. Application to Flexural Robotic Fingers

SMA wires are often applied to actuate flexure mechanisms [22–24]. However, the required pretension force of SMA would cause an initial deformation of flexure mechanisms. A pretensioner is presented to apply the pretension force without initially deforming a flexural mechanism. We illustrate here using a flexural robotic finger. Displacement self-sensing control experiments are conducted for demonstration.

4.1 Flexural finger and its pretensioner

SMA is an ideal actuator for flexural finger manipulators. Both distributed and concentrated actuation schemes can be employed, as shown in Fig. 13(a). Distributed actuation provides larger range to length ratio when compared with concentrated actuation. Based on the distributed actuation concept, Figs. 13(b–c) show the finger schematics [25]. The finger consists of a flexible beam, four straight columns, and an extension plate. The overall length of the finger is 10 mm and the length of the extension plate is 5 mm. The middle of each column has two holes to guide a V-shaped tendon. When the tendon is pulled by a SMA wire through its contraction, the finger deflects. Fig. 13(b) shows the original and deflected finger shapes. The tendon wire provides different direction of reaction forces at the columns of the finger. This resembles the actuation of many biological manipulators. The shape of finger segment is designed to curve inward to add the bending angle of the finger. The columns are also designed with isolators to prevent the tendon from contacting external objects and to provide larger contact surface. Fig. 13(d) shows two fingers gripping a foam.

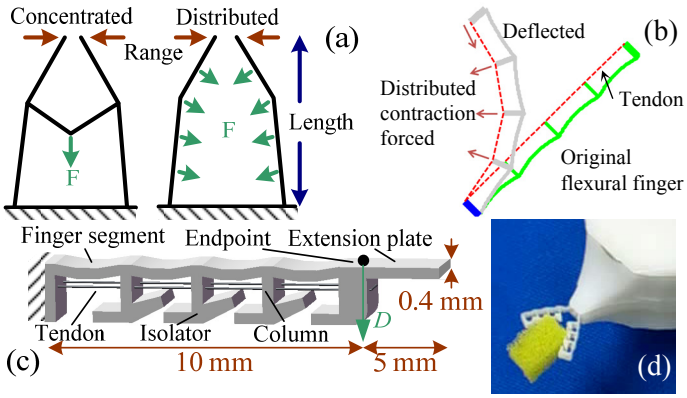

Fig. 13 (a) Concentrated and distributed actuation schemes (b) Original and deflected finger (c) CAD model of the finger (d) Two fingers gripping a foam

For practical finger manipulation, we choose the displacement of the finger endpoint as the quantity to be self-sensed. The previous studies show that a significant pretension force is required for accurate self-sensing, regardless of the quantities to be measured. When the tendon is directly actuated by SMA, the pretension force would result in an obvious initial deflection on the finger. This reduces the deflection capability of the flexure. Although the finger can be made more rigid to resist deflection, this would compromise the flexural motion.

To overcome this problem, Fig. 14 shows a design concept where an additional pretensioner joins the SMA wire and the tendon at a connector. The pretensioner is a serpentine flexure with dimension 24.6×27.6×10 mm. When in action, the SMA wire pulls the pretensioner with force (includes the two sides of a V-shaped wire) denoted as F_T. It is the sum of the pretention force F_p and SMA contraction force F.

$$F_T = F_p + F$$
$$\text{where } F_p = k_p \Delta x_p \text{ and } F = (k_p + k_f)\Delta x_c \quad (8)$$

The values k_p and k_f are the stiffnesses of the pretensioner and finger along the wire direction. To avoid finger initial deflection, the connector first displaces Δx_p to produce a pretension force F_p for the SMA wire. The finger tendon then attaches to the connector. When the wire contracts a distance Δx_c, its contraction force F acts on both the pretensioner and finger at the connector.

With the pretensioner, the pretension force of the SMA wire can be adjusted without initially deflecting the finger. Observing Eq. (8), the pretensioner stiffness must be large enough to provide sufficient pretension force. Meanwhile, it has to be smaller than the finger stiffness so that the majority of SMA contraction force goes to activate the finger. For the finger with k_f = 1084.4 N/m, the pretensioner stiffness is designed to be 386.2 N/m. The stiffnesses are obtained by using finite element simulation. They can be easily adjusted by changing the in-plane thickness of the flexure.

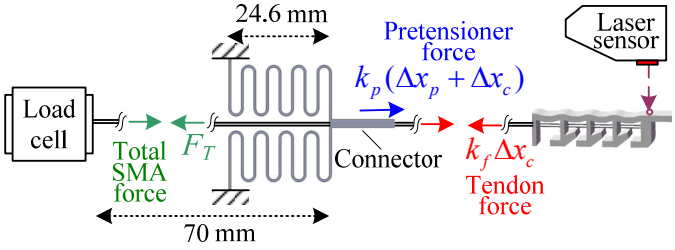

Fig. 14 Schematic of the pretensioner and finger

4.2 Effect of pretension force on finger displacement

With the aid of a pretensioner, an experiment is set up in Fig. 15 to study the self-sensing control of finger deflection. The pretensioner sits on Linear Stage 1 that can adjust the pretension force F_p. The finger sits on Linear Stage 2, which can set the finger tendon force to zero regardless of the pretension force. A load cell measures the pretension and contraction forces of the SMA wire and a laser displacement sensor (LK-081) measures the displacement of the finger's endpoint. The length of the V-shaped SMA wire is 7 cm.

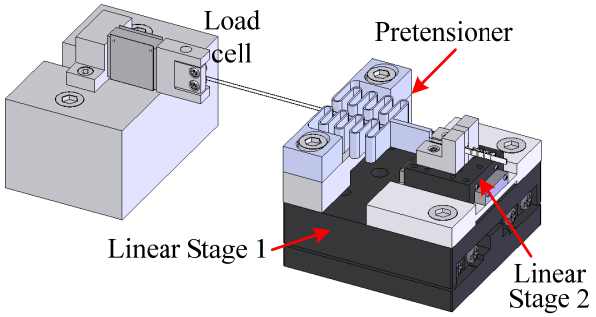

Fig. 15 Schematic of pretensioner set up

According to the results in Sec. II, larger pretension force can move the heating and cooling paths closer. We perform the same experiment again for the finger. The input sine wave voltage has 1/90 Hz. The displacement to resistance (*D-R*) curves for different pretension forces are shown in Fig. 16. It is observed that heating and cooling paths are closer with increasing pretension force of SMA wire, although not obvious as compared to those in Fig. 4.

For precise self-sensing control, the heating and cooling paths must be as close as possible. To study the closeness of heating and cooling paths of different pretension forces on a normal basis, we define the displacement gap for the endpoint of the finger, similar to those in Eq. (2).

$$\text{displacement gap} = \frac{1}{k}\sum_{i=1}^{k} \left| D_{hi} - D_{ci} \right| / D_{\max} \times 100\% \quad (9)$$

The relations between pretension force and displacement/force gaps are shown in Fig. 17. The larger the pretension force, the smaller the displacement gap is. When F_p is at 0.71 N, the displacement gap is the smallest. If the pretension force is too large, the heating and cooling curves have no intersection and move away from each other. We choose F_p = 0.71 N for the self-sensing control in the following section.

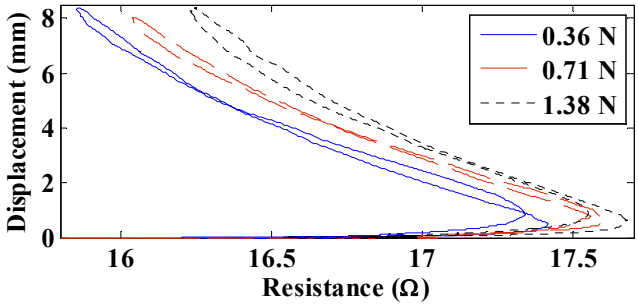

Fig. 16 Displacement curves of various F_p's (d = 100 μm)

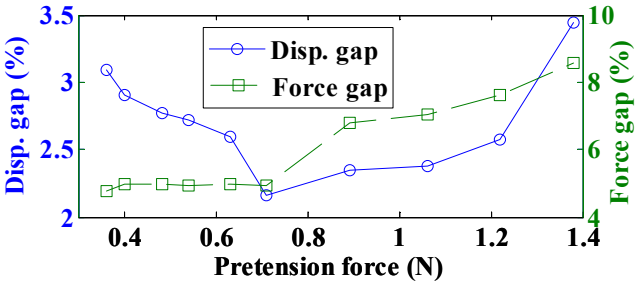

Fig. 17 Displacement gap versus pretension force (d = 100 μm)

4.3 Self-sensing finger Displacement control

By using the same polynomial model and fuzzy-tuned PID controller in Sec. III, Fig. 18 shows the results of step control experiment and the increment of each step is 0.5 mm with six seconds. The pretension force and displacement gap of the polynomial model are F_p = 0.71 N and 2.271%. The intentionally selected F_p moves the heating and cooling paths closer. Table 5 shows the detailed results of the experiment. The maximal *MAE* is 5.368% at D_{des} = 2.5 mm (return). The *MAE*'s at larger desired displacements are smaller than 2%.

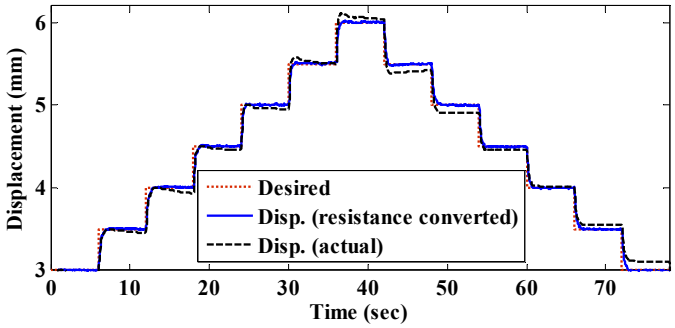

Fig. 18 Finger endpoint step response (F_p=0.71 N; d=100 μm)

Table 3 Numerical results of Fig. 18

Desired D (mm)	2.5	3.0	3.5	4.0	4.5	5.0	5.5	6.0
MAE - rise (%)	3.583	0.545	0.702	0.822	0.599	0.807	0.432	0.995
MAE - return (%)	5.368	3.599	1.450	0.432	0.910	1.958	1.697	

V. Conclusions

This paper has investigated and realized the self-sensing capabilities of SMA wire actuators. By measuring the resistance of SMA, the strain to resistance curves have been shown to be a better candidate for constructing self-sensing models, since they exhibit smaller hysteresis gaps than force to resistance curves. The hysteresis gap can be further reduced by pretensioning the SMA wire. Control experiments with a bias spring have indicated that the mean absolute error of using polyfitted self-sensing model is less than 2%.

A SMA actuated flexural finger is illustrated to demonstrate the self-sensing technique. In order not to initially deflect the finger, a pretensioner is inserted between the SMA wire and finger tendon. The finger tip displacement to SMA resistance model has been built for self-sensing control. After proper pretensioning, the finger deflection can be controlled with step response error less than 5%. Our future studies include the robustness of the self-sensing model to external disturbances so that the presented technique can be successfully applied to various SMA actuators.

References

[1] KF. Beyeler, A. Neild, S. Oberti, D. J. Bell, Y. Sun, J. Dual, and B. J. Nelson, 2007, "*Monolithically Fabricated Microgripper with Integrated Force Sensor for Manipulating Microobjects and Biological Cells Aligned in an Ultrasonic Field*," J. Microelectromech. Syst., **16**(1), pp. 7–15.

[2] T. C. Duc, G. K. Lau, J. F. Creemer, and P. M. Sarro, 2008, "*Electrothermal Microgripper with Large Jaw Displacement and Integrated Force Sensors*," J. Microelectromech. Syst., **17**(6), pp. 1546–1555.

[3] S. Konishi, F. Kawai, and P. Cusin, 2001, "*Thin Flexible End-effector Using Pneumatic Balloon Actuator*," Sens. Actuators A, **89**, pp. 28–35.

[4] R. Lumia and M. Shahinpoor, 2008, "*IPMC Microgripper Research and Development*," J. Phys.: Conf. Ser., **127**, 012002.

[5] R. Pérez, J. Agnus, C. Clévy, A. Hubert, and N. Chaillet, 2005, "*Modeling, Fabrication, and Validation of a High-Performance 2-DoF Piezoactuator for Micromanipulation*," IEEE/ASME Trans. Mechatron., **10**(2), pp. 161-171.

[6] D.-H. Kim, B. Kim, and H. Kang, 2004, "*Development of a Piezoelectric Polymer-based Sensorized Microgripper for Microassembly and Micromanipulation*," Microsystem Technologies, **10**, pp. 275–280.

[7] Z. W. Zhong and C. K. Yeong, 2006, "*Development of a Gripper Using SMA Wire*," Sens. Actuators A, **126**(2), pp. 375–381.

[8] J. H. Kyung, B. G. Ko, Y. H. Ha, and G. J. Chung, 2008, "*Design of a Microgripper for Micromanipulation of Microcomponents Using SMA Wires and Flexible Hinges*," Sens. Actuators A, **141**, pp. 144–150.

[9] M. R. Bai and H. Wu, 1999, "*Robust Control of a Sensorless Bass-enhanced Moving-coil Loudspeaker System*," J. Acoust. Soc. Am., **105**, pp. 3283–3289.

[10] M. Gurjar and N. Jalili, 2007, "*Toward Ultrasmall Mass Detection Using Adaptive Self-sensing Piezoelectrically Driven Micro cantilevers*," IEEE/ASME Trans. Mechatron., **12**, pp. 680–688.

[11] A. Punning, M. Kruusmaa, and A. Aabloo, 2007, "*A Self-sensing Ion Conducting Polymer Metal Composite (IMPC) Actuator*," Sens. Actuators A: Physical, **136**, pp. 656–664.

[12] P. Eyabi and G. Washington, 2006, "*Modeling and Sensorless Control of an Electromagnetic Valve Actuator*," Mechatronics, **16**, pp. 159–175.

[13] D. C. Lagoudas, 2008, "*Shape Memory Alloys: Modeling and Engineering Application*," New Yourk: Springer.

[14] H. J. Lee and J. J. Lee, 2000, "*Evaluation of the Characteristic of a Shape Memory Alloy Spring Actuator*," Smart Mater. Struct., **9**, pp. 817–820.

[15] S. M. Dutta and F. H. Ghorbel, 2005, "*Differential Hysteresis Modeling of a Shape Memory Alloy Wire Actuator*," IEEE/ASME Trans. Mechatron., **10**, pp. 189–197.

[16] N. Ma, G. Song, and H. Lee, 2004, "*Position Control of Shape Memory Alloy Actuators with Internal Electrical Resistance Feedback Using Neural Networks*," Smart Mater. Struct., **13**, pp. 777–783.

[17] K. Malukhin and K. F. Ehmann, 2008, "*An Experimental Investigation of the Feasibility of "self-sensing" Shape Memory Alloy Based Actuators*," ASME J. Manuf. Sci. Eng., **130**, 031109-1.

[18] S.-H. Liu, T.-S. Huang, and J.-Y. Yen, 2010, "*Tracking Control of Shape-Memory-Alloy Actuators Based on Self-Sensing Feedback and Inverse Hysteresis Compensation*," Sensors, **10**, pp. 112–127.

[19] www.dynalloy.com/

[20] B. K. Nguyen and K. K. Ahn, 2007, "*Internal Model Control for Shape Memory Alloy Actuators Using Fuzzy Based Preisach Model*," Sen. Actuators A, **136**, pp. 730–741.

[21] A. Kumagi, T. Liu, and P. Hozian, 2006, "*Control of Shape Memory Alloy Actuators with a Neuro-fuzzy Feedforward Model Element*," Intelligent Manufacturing, **17**, pp. 45–56.

[22] S. G. Shu, D. C. Lagoudas, D. Hughes, and J. T. Wen, 1997, "*Modeling of a Flexible Beam Actuated by Shape Memory Alloy Wires*," Smart Mater. Struct., **6**, pp. 265–277.

[23] Q. Chen and C. Levy, 1996, "*Active Vibration Control of Elastic Beam by Means of Shape Memory Alloy Layers*," Smart Mater. Struct., 5, pp. 400–406.

[24] M. Sreekumar and M. Singaperumal, 2009, "A Generalized *Analytical Approach to the Coupled Effect of SMA Actuation and Elastica Deflection*," *Smart Mater. Struct.,* **18**, 115026.

[25] C.-M. Lin, C.-H. Fan, and C.-C. Lan, 2009, "*A Shape Memory Alloy Actuated Microgripper with Wide Handling Ranges*," Proc. IEEE/ASME AIM, pp. 12-17.